# Nano-Micro Letters

**ARTICLE**

# Fabricating Na/In/C Composite Anode with Natrophilic Na–In Alloy Enables Superior Na Ion Deposition in the EC/PC Electrolyte

Hui Wang[1,2], Yan Wu[2], Ye Wang[1], Tingting Xu[1], Dezhi Kong[1], Yang Jiang[3], Di Wu[1], Yongbing Tang[4], Xinjian Li[1] ✉, Chun-Sing Lee[2] ✉

## HIGHLIGHTS

- Na/In/C composite anode tailored with natrophilic NaIn and $Na_2In$ phases was constructed via a facile molten metal immersion method.

- Long-term Na ion plating/stripping stability in the common ethylene carbonate/propylene carbonate electrolyte was achieved with Na/In/C anode.

- Na ion deposition reversibility of Na/In/C anode was analyzed by in situ microscope, ab initial molecular dynamics and finite element simulations.

**ABSTRACT** In conventional ethylene carbonate (EC)/propylene carbonate (PC) electrolyte, sodium metal reacts spontaneously and deleteriously with solvent molecules. This significantly limits the practical feasibility of high-voltage sodium metal batteries based on Na metal chemistry. Herein, we present a sodium metal alloy strategy via introducing NaIn and $Na_2In$ phases in a Na/In/C composite, aiming at boosting Na ion deposition stability in the common EC/PC electrolyte. Symmetric cells with Na/In/C electrodes achieve an impressive long-term cycling capability at 1 mA cm$^{-2}$ (> 870 h) and 5 mA cm$^{-2}$ (> 560 h), respectively, with a capacity of 1 mAh cm$^{-2}$. In situ optical microscopy clearly unravels a stable Na ion dynamic deposition process



on the Na/In/C composite electrode surface, attributing to a dendrite-free and smooth morphology. Furthermore, theoretical simulations reveal intrinsic mechanism for the reversible Na ion deposition behavior with the composite Na/In/C electrode. Upon pairing with a high-voltage NaVPOF cathode, Na/In/C anode illustrates a better suitability in SMBs. This work promises an alternative alloying strategy for enhancing Na metal interfacial stability in the common EC/PC electrolyte for their future applications.
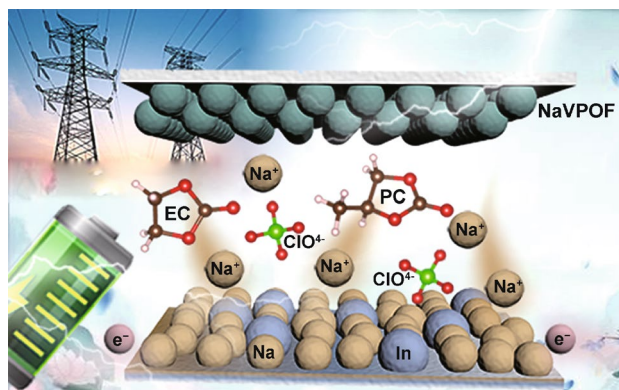
**KEYWORDS** EC/PC electrolyte; Sodium metal batteries; Na/In/C electrode; Dendrite-free and smooth morphology; Theoretical simulations

✉ Xinjian Li, lixj@zzu.edu.cn; Chun-Sing Lee, apcslee@cityu.edu.hk
[1] Key Laboratory of Material Physics of Ministry of Education, School of Physics and Microelectronics, Zhengzhou University, Zhengzhou 450052, People's Republic of China
[2] Department of Chemistry, Center of Super-Diamond and Advanced Films (COSDAF), City University of Hong Kong, Hong Kong SAR 999077, People's Republic of China
[3] School of Materials Science and Engineering, Hefei University of Technology, Hefei 230009, Anhui, People's Republic of China
[4] Shenzhen Institutes of Advanced Technology, Chinese Academy of Sciences, Shenzhen 518055, People's Republic of China

# 1 Introduction

Beyond traditional intercalation chemistry, advanced lithium metal batteries (LMBs) systems, such as Li–S [1–4] and Li-O$_2$ [5, 6], have dramatically boosted the energy density of lithium-ion batteries. Nevertheless, high cost and scarcity of metallic lithium largely stifle the feasibility of LMBs [7, 8]. Comparatively, by virtue of materials abundance, competitive theoretical capacity (1166 mAh g$^{-1}$) and desirable redox potential ($-2.71$ V vs. the standard hydrogen potential), sodium metal batteries (SMBs) provide an appealing alternative for LMBs [9–11, 11]. As a result, this has prompted burgeoning research interest on SMBs, such as Na–S/Se/Te [12–19], Na–O$_2$ [19–21] and Na–P [22–24] systems.

Albeit with these collective attributes, the deployment of Na metal still confronts huge challenges including catastrophically safety issues and poor cycling reversibility. First, owing to its lower Lewis acidity and larger atomic radius, Na metal reacts much more severely with flammable organic liquid electrolytes than Li metal [25, 26]. Second, non-uniform Na ion platting and stripping often lead to electrochemical and/or morphological instabilities [27–33]. All of these problems would cause various unwanted consequences such as electrolyte depletion, detrimental Na dendritic growth, large volume variation, inferior Coulombic efficiency (CE), poor quality SEI (solid electrolyte interphase) and ultimately cells' failure. Thus far, unremitting efforts have been dedicated to restrict Na dendritic proliferation and improve long-term cyclability. These include modifying molecular structure of electrolytes [34], fabricating protective surface coating [35, 36], building steady artificial SEI [37], synthesizing novel Na ion deposition substrates [38, 39], innovating liquid Na–K alloy [30] and designing robust solid-state electrolytes (SSEs) [40–42]. These rational approaches undoubtedly enhance Na ion deposition stability, while challenge still remains regarding to Na dendrite issues and fabrication complexity. Particularly, (i) ether-based electrolytes can easily decompose at potentials above ~3.8 V for SIBs (above ~4.0 V for lithium-ion batteries) and thus would compromise cells' working voltages and energy densities [43]; (ii) unsatisfactory interfacial compatibility between Na metal and SSEs as well as Na dendritic growth within the SSEs necessitate further enhancements [40]. In comparison, by virtue of antioxidant capability, easy tunability and low cost, EC/PC electrolyte has better prospects for fabricating high-voltage SMBs. Nevertheless, continuous parasitic reactions between aggressive Na metal and EC/PC electrolyte still occur regardless of artificial SEI, surface coating and additives [44]. In this sense, tailoring Na metal anode to be more compatible with ester-based electrolytes is strongly desirable for the implementation of viable SMBs with high operating potentials and energy densities.

In this manuscript, we prepare a Na/In/C composite to further stabilize Na metal anode in the EC/PC electrolyte. In doing so, symmetric cells with Na/In/C electrodes can yield superior operational life spans at 1 ($>870$ h), 2 ($>710$ h) and 5 ($>560$ h) mA cm$^{-2}$, respectively, with a capacity of 1 mAh cm$^{-2}$. Stable Na ion deposition behavior is also evidenced at a higher capacity of 3 mAh cm$^{-2}$. Scanning electron microscopy (SEM) and in situ optical microscopy results clearly demonstrate that Na ions smoothly deposited upon the Na/In/C surface without any sodium dendrites. On the contrary, porous and dendritic morphology is observed on a pure Na metal surface after 5 min deposition at 1.0 mA cm$^{-2}$. Ab initial molecular dynamics (AIMD) simulation, density functional theory (DFT), finite element (FE) calculations and electrochemical analysis clearly unveil that the presence of In promotes Na ions nucleation dynamics and deposition stability. Moreover, when paired with a high-voltage Na$_3$V$_2$O$_2$(PO$_4$)$_3$ cathode (up to 4.3 V), the sodium metal full cells utilizing Na/In/C anode demonstrate a much more promising capacity retention upon extensive cycles. All of these comprehensive results establish a deep insight into the construction of Na/In/C composite anode to improve the cycling stability of SMBs.

# 2 Experimental Section

## 2.1 Fabrication of Na/In/C Composite Electrode

Typically, a piece of carbon cloth was initially cut into circular disks of ~1 cm diameter via a punch machine. Then, these disks were totally immersed into ethanol with an ultrasonication treatment for 3 h. Next, the plates were dried at 80 °C under vacuum for 24 h. Subsequently, metal Na foil, metallic In powder and carbon cloth disks (weight ratio of Na:In:C = 10:1:4) were put into a nickel crucible maintaining at ~400 °C for 10 min. Finally, liquefied Na and In can thoroughly infuse into the entire carbon cloth plate, creating

the Na/In/C composite. Average weight of one Na/In/C composite disk ($0.785\ cm^{-2}$) is 9.3 mg, and the mass loading of Na within the Na/In/C composite is $7.9\ mg\ cm^{-2}$.

## 2.2 Synthesis of $Na_3V_2O_2(PO_4)_2F$ (NaVPOF)

Briefly, 0.1 g hexadecyl trimethyl ammonium bromide (CTAB) were firstly added into 36 mL DMF and sonicated for 20 min. Secondly, a solution comprising of 0.0015 mol NaF, 0.001 mol $NH_4VO_3$ and 8 mL deionized water was gradually drop-wisely into DMF. Then, 8 mL $(NH_4)_2HPO_4$ (0.001 mol) aqueous solution was mixed with the above solution to guarantee the required stoichiometric ratio (Na:V:P:F = 3:2:2:3). Finally, this solution was sealed into the 60-mL Teflon autoclaves and retained at 180 ℃ for 10 h.

## 2.3 Materials Characterization

X-ray diffractometer (XRD) patterns of Na, Na/In/C and NaVPOF were obtained with an X-ray diffractometer utilizing Cu-K radiation. A QUATTRO S scanning electron microscope was employed to obtain the morphology and microstructure of the cycled Na and Na/In/C electrodes. X-ray photoelectron spectroscopy (XPS, VG ESCALAB 220i-XL) was carried out to investigate surface chemical properties of the cycled Na and Na/In/C electrodes. Real-time Na ion dynamics deposition and surface morphology evolution process on the Na and Na/In/C electrode were studied by in situ optical microscopy.

## 2.4 Electrochemical Measurements

To assess the Na ion stripping/plating stability, symmetrical Na||Na and Na/In/C||Na/In/C cells were assembled in a glove box. Electrochemical deposition curves and long-term cycling life span of these cells were tested with a MACCOR battery cycler at 1, 2 and $5\ mA\ cm^{-2}$ with a capacity of 1 and $3\ mAh\ cm^{-2}$. As to the full-cell testing, NaVPOF, carbon black and polyvinylidene fluoride with a weight ratio of 8:1:1 were leveraged as active material, conductive additive and binder, respectively. 1.0 M $NaClO_4$ in EC/PC (1:1 volume ratio) with 5 wt% fluoroethylene carbonate (FEC) was adopted as electrolyte. Mass loading of the NaVPOF cathode/pure Na foil anode is $14.2/7.9\ mg\ cm^{-2}$. Cyclic voltammetry (CV) measurements were taken with a Zahner electrochemical workstation (voltage range of 2.5–4.3 V, $0.5\ mV\ s^{-1}$ scan rate) to study the Na ion deposition kinetics and redox reversibility. Rate performance and long-term cycling stability tests were done from 0.05 C to 5 C rates. Interfacial electrochemical impedance spectroscopy (EIS) features were determined over a frequency range from 1 MHz to 100 mHz through an impedance analyzer (Zennium pro).

## 2.5 Computational Details

DFT simulations were firstly conducted to determine Na atom adsorption sites, binding energies and charge differential density upon (100), (110) and (111) crystal planes of Na metal and NaIn as well as (311) crystal plane of $Na_2In$. All the DFT calculations were coped with projector augmented plane wave method [45]. The exchange–correlation interaction among itinerant electrons is handled by the Perdew–Burke–Ernzerhof (PBE) functional [46]. van der Waals interactions between Na atom and Na metal or NaIn/$Na_2In$ surface were treated with semiempirical London dispersion corrections of Grimme et al. [47]. Cutoff energy of the plane wave basis was set at 600 eV to ensure strict force and energy convergence criterion, and the k-point mesh (Monkhorst–Pack) was $7 \times 7 \times 1$. AIMD simulations were then performed to clarify dynamic Na atoms movement process on the (011) crystal surface of Na metal and NaIn. A lattice matching interface consisting of six layers of NaIn and three layers of Na metal were fabricated. All the AIMD simulations were done with Gaussians and plane wave (GPW) method implemented in the CP2K software package with a single Γ point and the energy cutoff was set at 300 Ry [48]. DFT-D3 and PBE were employed to deal with long-range weak van der Waals and electron exchange–correlation interactions. All the configurations were allowed to relax for 1.2 ps (time step is 0.5 fs) at 300 K in the canonical ensemble (NVT) dictated by Nose–Hoover thermostat. Morphology evolution of Na metal surface with distinct overpotential and bump shape was further investigated using finite element simulation (COMSOL Multiphysics) utilizing tertiary current distribution and deformed geometry modules. The Na ion deposition kinetics at the Na or Na/In surface were subjected to the concentration-dependent Butler–Volmer equation:

$$i = i_0\left[c_R * exp\left(\alpha_a F\eta/RT\right)i_0 - c_O * exp\left(-\alpha_c F\eta/RT\right)\right] \quad (1)$$

where $i_0$ stands for the exchange current density; $c_R$ and $c_O$ are the concentrations of the oxidized and reduced species (initial concentration of Na ion in the electrolyte is 1 M), respectively; upon deposition process, $c_R$ maintains constant (1 M), while the value of $c_O$ is given according to Nernst–Planck equation as described before [49]; value of the $\alpha_a$ and $\alpha_c$ is 0.5, respectively; and $\eta$, R and T are the overpotential, gas constant and temperature, respectively. Therefore, Na metal surface deposition behavior can be obtained based on Faraday's law of electrolysis:

$$V = -Mi/\rho Fn \quad (2)$$

$\rho$ and M are the density and molar mass of Na metal, respectively.

# 3 Results and Discussion

## 3.1 Microstructure and Morphology Characterizations

As depicted in Fig. 1a, the Na/In/C composite was fabricated via a facile Na/In molten metal infusion method with a carbon cloth as the accommodation matrix and a subsequent condensation process (Na:In:C = 10:1:4 by weight). Driven by hybrid entropy and good wettability of the substrate, carbon cloth is uniformly covered by the molten Na/In metal, rendering a flat electrode surface similar to pure Na metal surface as presented in Fig. 1b-d. As shown in Fig. S2, XRD peaks confirm the existence of cubic NaIn and orthorhombic Na₂In apart from the typical diffraction peaks of cubic Na metal. Furthermore, as shown in Fig. 1e, elemental mapping images confirm the uniform distributions of Na and In within the whole composite electrode.

## 3.2 Electrochemical Testing of the Na Ion Deposition

Na ion plating/stripping properties of the Na/In/C and the pure Na metal were subsequently evaluated with symmetrical coin cells. 1.0 M NaClO₄ in EC:PC (1:1 by volume) with 5 wt% FEC was employed as an electrolyte. As shown in Fig. 2a, c, cells cycled galvanostatically at 1 and 2 mA cm⁻² (1 mAh cm⁻²) demonstrated stable deposition overvoltage of 51/100 mV and smooth voltage profiles over 870/710 h, respectively. Intriguingly, even under a harsh condition of 5 mA cm⁻² (Fig. 2e), the cell still has a long-term cycling life over 560 h. Of note, upon extensive cycling process at
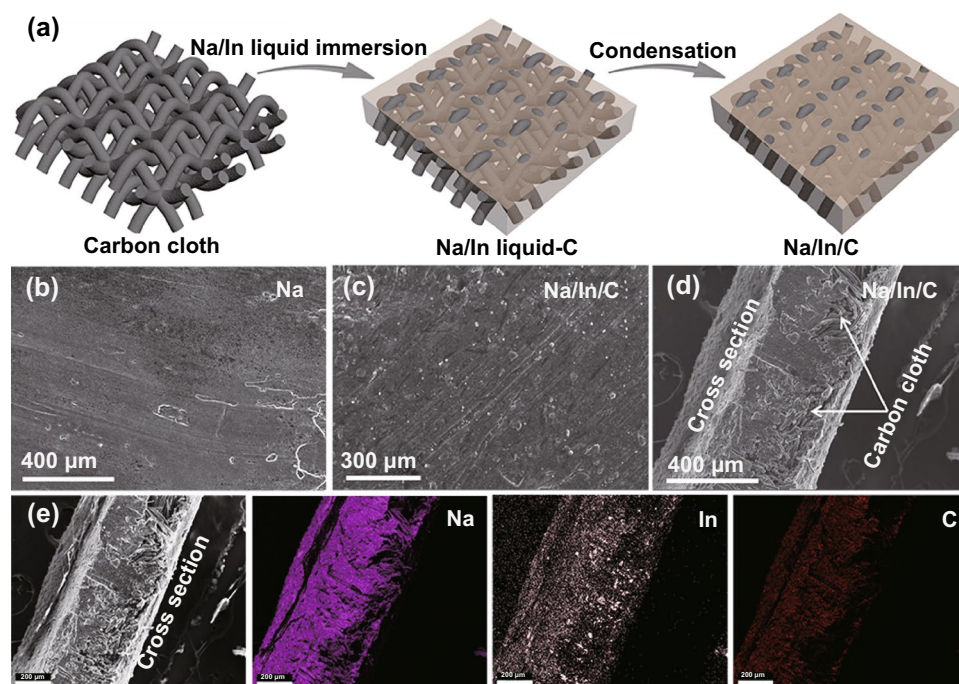


**Fig. 1** **a** Schematic image of the fabrication process of the Na/In/C composite. **b, c** SEM images of the pure Na metal the Na/In/C composite. **d** Cross-sectional SEM images of the Na/In/C composite. **e** Element mappings of the synthesized Na/In/C composite anode

5 mA cm$^{-2}$, a thick SEI with relative low quality (compared with 1 and 2 mA cm$^{-2}$) and gradually increasing thickness will cover the whole anode surface [50], hence resulting in the formation of protrusions and islands (Fig. S3b, c) as well as slow Na ion transport kinetics within the SEI (Fig. S3a). As a result, larger overpotential would be needed to maintain a constant applied deposition current based on the Butler–Volmer equation, thereby leading to a progressively increasing overvoltage as presented in Fig. 2e [51]. It is also

remarkable that cells with the Na/In/C electrode can also deliver a long life span over 300 h at 1 and 2 mA cm$^{-2}$ with a higher capacity of 3 mAh cm$^{-2}$ as shown in Fig. S4a, b. Moreover, even at a harsh testing condition of 5 mAh cm$^{-2}$, the Na/In/C electrode can still retain an impressive cycling stability over 600/300 h at 1 and 5 mA cm$^{-2}$ (Figs. 2g and S4c). Notably, the Na/In/C electrode demonstrates better stabilities among recently reported Na metal batteries cycled in the common EC/PC electrolyte (Fig. S5). By comparison, as
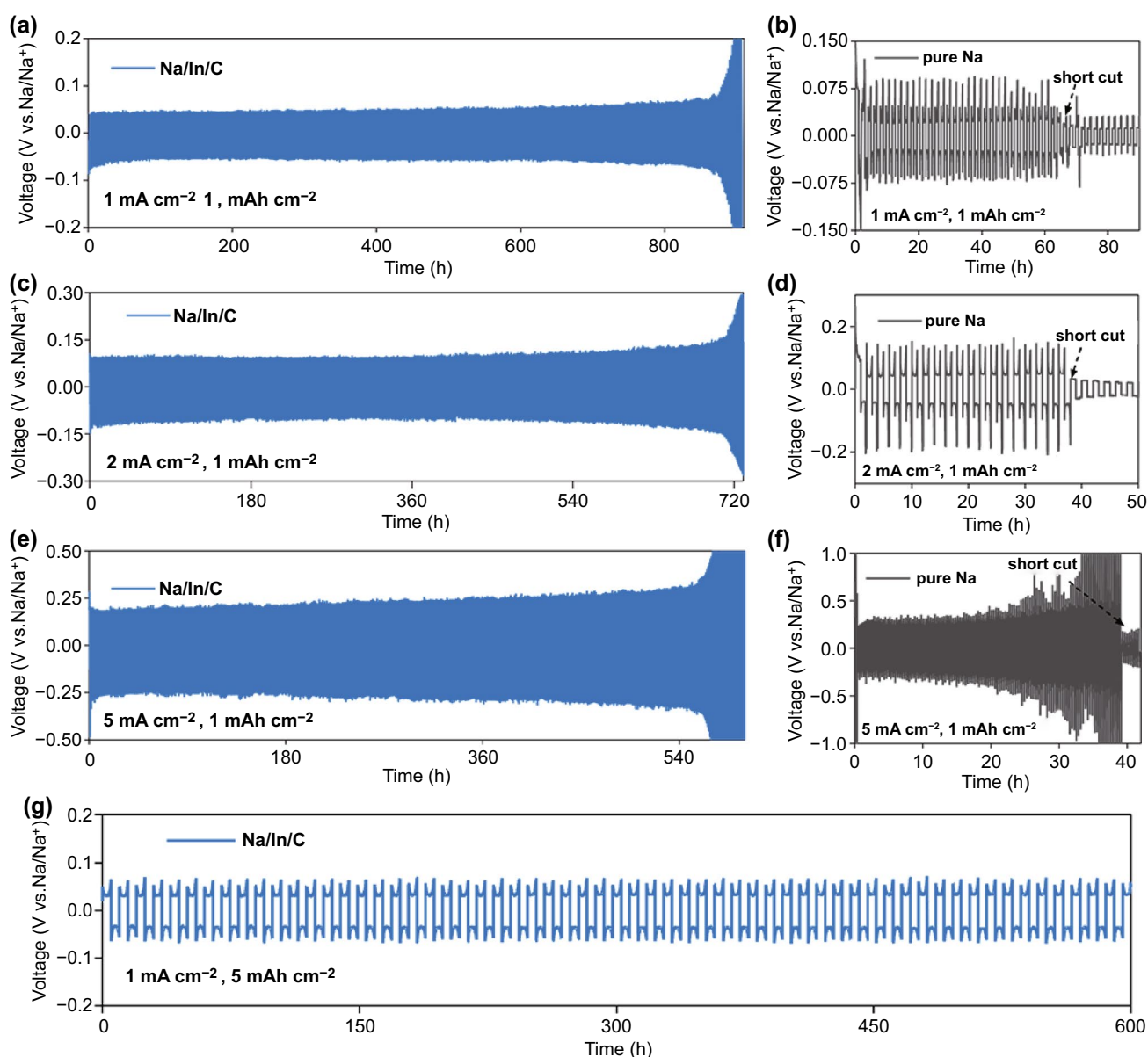


**Fig. 2** **a, c, e** Long-term Na ion plating/stripping profiles of the Na/In/C composite symmetrical cells at 1, 2 and 5 mA cm$^{-2}$ with a capacity of 1 mAh cm$^{-2}$. **b, d, f** Cycling performances of symmetrical cells assembled with pure Na metal at 1, 2 and 5 mA cm$^{-2}$ with a capacity of 1 mAh cm$^{-2}$. **g** Long-term Na ion deposition profiles of the Na/In/C composite symmetrical cell at 1 mA cm$^{-2}$ with a high capacity of 5 mAh cm$^{-2}$

illustrated in Fig. 2b, d, f, it can be seen that cells assembled with pure Na metal electrodes experience much larger voltage hysteresis of 82, 156 and 340 mV at 1, 2 and 5 mA cm$^{-2}$ (1 mAh cm$^{-2}$). Even worse, these cells all display an abrupt voltage drop (Fig. 2b, d, f,) in a few cycling hours, indicative of the soft short circuit originated from penetration by notorious sodium dendrites. Moreover, rate capability of the symmetrical Na/In/C and Na cells are depicted in Fig. 3a. Apparently, as the current density changing from 1 to 5 mA cm$^{-2}$, the cell utilizing Na/In/C composite electrodes show low voltage fluctuation and highly stable Na ion deposition. In parallel, long-term cycling stabilities of cells employing Na/In/C anodes with different Na:In weight ratios (8:1 and 12:1) were also evaluated. As shown in Fig. S6a, d, both Na/In/C samples (8:1 and 12:1) demonstrate the distinct presence of natrophilic NaIn and Na$_2$In phases. As to the Na/In/C anode with a ratio of 12:1, it is obvious that cells show large voltage fluctuations and unstable charge/charge profiles at 1 and 5 mA cm$^{-2}$ (1 mAh cm$^{-2}$) (Fig. S6b, c). This could be mainly ascribed to the reduced natrophilic NaIn and Na$_2$In phases compared with Na/In/C anode with a ratio of 10:1. Albeit cells utilizing Na/In/C anode (8:1) can deliver similar cycling stability at 1 and 5 mA cm$^{-2}$ (1 mAh cm$^{-2}$) (Fig. S6e, f) as those employing Na/In/C anode (10:1), fabricating Na/In/C anode with a ratio of 10:1 is much more preferable on account of higher prices of In.

As expected, cell with pure Na metal exhibits a poor tolerance to the rate testing condition and a sudden voltage drop associated with short circuit occurs (Fig. 3a), meaning that Na metal undergoes a much more severe corrosion in the EC/PC electrolyte. Under the 2 and 5 mA cm$^{-2}$ testing (1 mAh cm$^{-2}$) conditions, it can be witnessed that cells with the Na/In/C composite electrodes demonstrate a much smaller nucleation overpotential entailed for Na ion plating comparing with the cells with pure Na metal electrodes (Fig. S7a-d). Interestingly, it is found that the pure Na metal and the Na/In/C anode possess similar growth overpotentials (Na: ~ 25 mV, Na/In/C: ~ 20 mV) at 1 mA cm$^{-2}$ in the initial tens of cycles (Fig. 3b, c), which may originate from their similar SEI thicknesses and Na ion diffusion kinetics within SEI under a low Na ion deposition current [50]. However, upon long-term cycling process, reactive Na metal demonstrates unstable Na ion deposition process and even short cut, which can be largely attributed to the poor SEI quality and dendrites formation as shown schematically in Fig. S8. This suggests that the Na–In alloy can significantly decrease Na ion nucleation barrier and promote Na ion nucleation and propagation kinetics [10].

Electrochemical impedance of the symmetric cells with Na/In/C and Na metal electrodes was further measured with EIS. Figure 3d, e shows Nyquist plots of the Na/In/C‖Na/In/C cells and Na‖Na cells after 1, 60 and 120 cycles at 1 mA cm$^{-2}$ (1 mAh cm$^{-2}$). From 60 to 120 cycles, EIS profiles for Na/In/C‖Na/In/C cells show little changes, while those of the Na‖Na cells change significantly. $R_{SEI}$ and $R_{ct}$, representing SEI quality and charge transfer dynamics, were obtained by fitting the corresponding EIS profiles as manifested by Fig. S9a, b. Clearly, cell with the Na/In/C composite electrode presents low $R_{SEI}$ of 21.75 Ω and $R_{ct}$ of 71.44 Ω (Fig. S9a) after initial cycling. After 60 and 120 cycles, these $R_{SEI}$ and $R_{ct}$ values undergoes only mild increases upon cycling. In contrast, although the cell with Na metal electrode demonstrates a similar $R_{SEI}$ (23.86 Ω) and $R_{ct}$ of 72.89 Ω (Fig. S9a) after first cycle, conspicuous increases in $R_{SEI}$ and $R_{ct}$ values are shown in Fig. S9b after 60 and 120 cycles, indicating that the Na/In/C electrodes possess much improved charge transfer dynamics and better chemical stability in the common EC/PC electrolyte.

### 3.3 Morphology Variation and Surface Analyses

Morphological evolutions of the Na metal and the Na/In/C composite electrode after various cycles (1 mA cm$^{-2}$, 1 mAh cm$^{-2}$) were investigated using SEM and in situ optical microscopy. As shown in Fig. 4a-c, dendritic and porous Na deposition emerges after 50 and 100 cycles, which can be further revealed by in situ optical microscopy visualizing the deposited Na surface (Fig. 4g). On the contrary, the Na/In/C electrode preserves a dendrite-free and unscathed morphology after 100 and 500 cycles (Fig. 4d-f). Upon cycling at higher current densities of 2 and 5 mA cm$^{-2}$ (Fig. S10a-f), the Na/In/C composite electrode maintains similar morphologies as that cycled at 1 mA cm$^{-2}$ (Fig. 4d-f), while pure Na metal anode suffers from alike dendritic and porous Na deposition after 100 and 500 cycles (Fig. S11a-f). Besides, in situ optical microscopy (Figs. 4h and S10g, h) shows that the Na/In/C surface is smooth without forming any detectable sodium protuberance and dendrite, again confirming remarkable interfacial stability of the Na/In/C electrode in the EC/PC electrolyte.
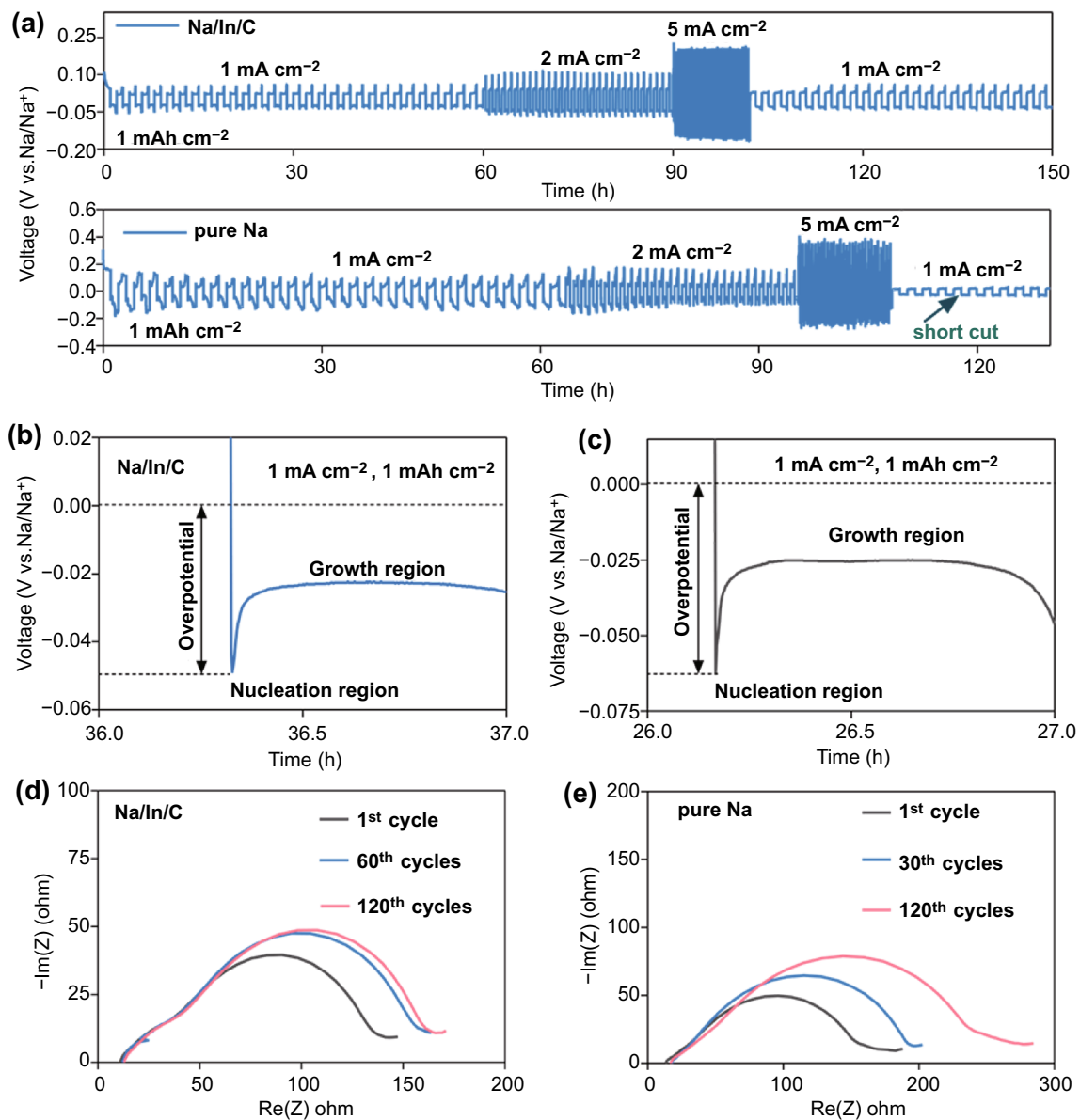
**Fig. 3 a** Rate performances of the symmetric cells assembled with the Na/In/C composite and Na metal at 1, 2 and 5 mA cm$^{-2}$. **b, c** Nucleation overpotentials for Na ion deposition in Na/In/C||Na/In/C and Na||Na cells at a current density of 1 mA cm$^{-2}$, 1 mAh cm$^{-2}$. **d, e** Electrochemical impedance analyses of the Na/In/C||Na/In/C cells and the Na||Na cells after 1, 60 and 120 cycles

Other than the post-cycling morphology evolution analysis, interfacial chemistry of the Na and the Na/In/C composite electrodes after 50 cycles at 1 mA cm$^{-2}$ (1 mAh cm$^{-2}$) was studied with XPS (Figs. 5 and S12). As shown in the C 1 s spectra of the pure Na metal (Fig. 5d), several clear peaks located at 286.7, 288.9 and 290.4 eV can be assigned to -C-O-, ROCO$_2$Na and Na$_2$CO$_3$ [39]. Interestingly, except the existence of the above products, it was worth mentioning that one extra peak at 292.5 eV related to –CF$_3$ can

be observed in the C 1 s spectra of the Na/In/C electrode (Fig. 5a). Apart from this difference, C 1 s signals associated with the decomposed carbonate electrolyte are stronger for the pure Na electrode. Additionally, compared with pure Na metal (Fig. 5e, f), the Na/In/C electrode demonstrates an intensive signal of the F 1 s (Fig. 5c) and Cl 2p spectra (Fig. 5b), suggesting apparent enrichments of NaF and NaCl products in the SEI component [51]. The absence of F signal of the pure Na metal anode after 50 cycles can be
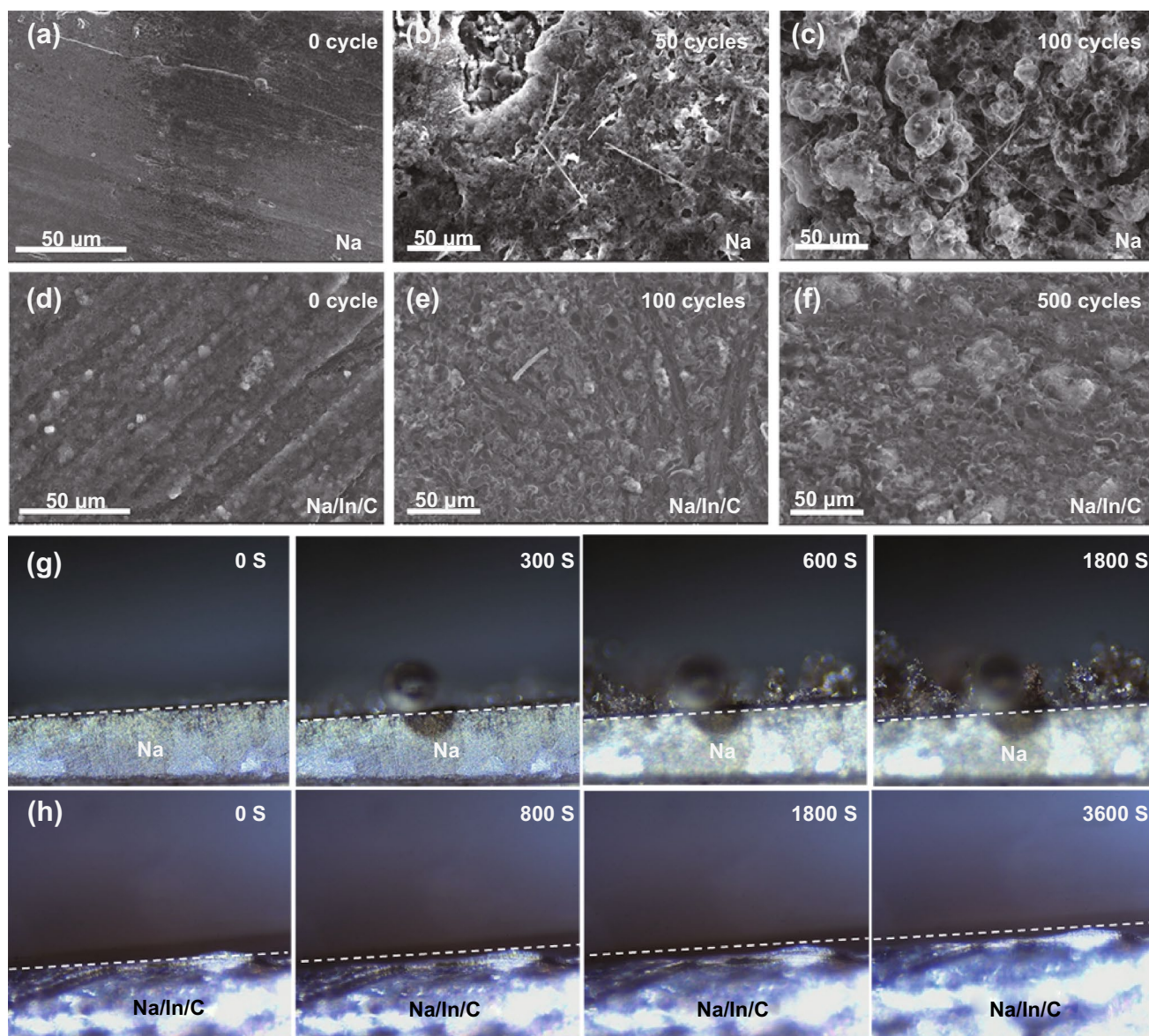
**Fig. 4** **a–c** SEM images of the cycled Na metal anode at 1 mA cm$^{-2}$ with a capacity of 1 mAh cm$^{-2}$ after 0, 50 and 100 cycles. **d-f** SEM images of the cycled Na/In/C composite electrode at 1 mA cm$^{-2}$ with a capacity of 1 mAh cm$^{-2}$ after 0, 100 and 500 cycles. **g, h** In situ optical microscopic images of Na ion deposition process on pure Na metal and the Na/In/C composite electrode at 1 mA cm$^{-2}$, 1 mAh cm$^{-2}$

largely attributed to the continuous breaking of SEI on the Na dendrite structures (Figs. 4a-c and S11a-f, S13), leading to the unnecessary consumption of electrolyte and thus causing ultralow contents of preferable NaF and –CF$_3$ [51]. Furthermore, it is apparent that peaks located at 441.3/441.6 and 449.2/449.8 eV (Fig. S14) can be ascribed to the presence of natrophilic NaIn and Na$_2$In phases on the Na/In/C composite electrode interface [52], which are conducive to promoting Na ion deposition stability as verified by both

experimental analyses and DFT simulations. It is thus reasonable to consider that the Na/In/C electrode possesses a much more robust SEI structure and interface stability in the EC/PC electrolyte. According to the above analyses, it is reasonably accepted that Na ions preferentially deposit at the protuberances upon cycling (Fig. 5g), which ultimately result in the formation of cracks and dendrites. By contrast, the presence of In can improve Na ion nucleation kinetics and guide uniform Na ion deposition (Fig. 5g), thus
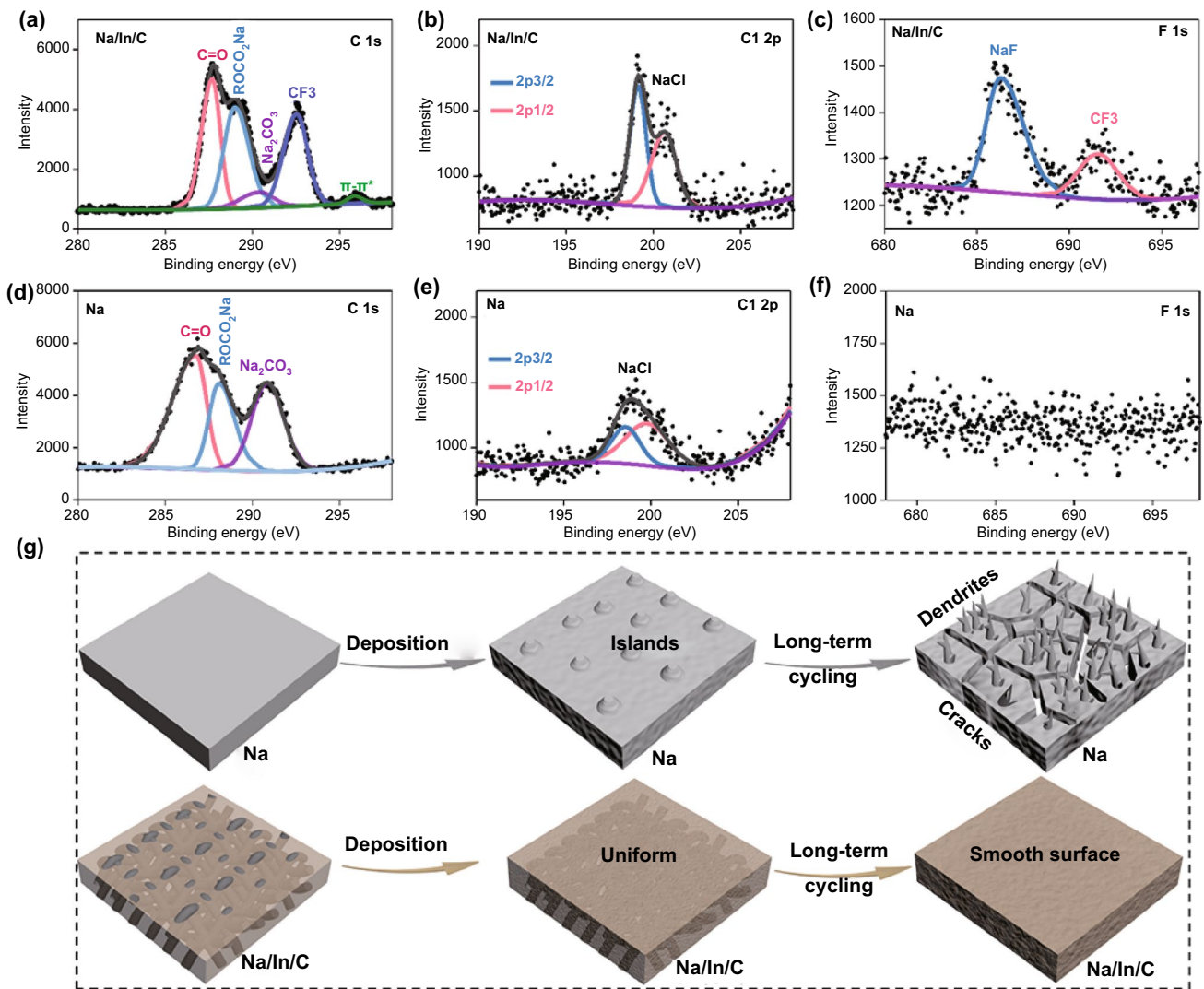
**Fig. 5** High-resolution XPS profiles: **a, d** C 1 s, **b, e** Cl 2p and **c, f** F 1 s of the Na metal and the Na/In/C composite electrodes after 50 cycles at 1 mA cm$^{-2}$, 1 mAh cm$^{-2}$. **g** Schematic of Na ion deposition behavior on a pure Na metal anode and a Na/In/C composite anode. Na ion tends to selectively deposit on defects and protruded area leading to the formation of cracks and dendrites for pure Na anode, while Na ions prefer to smoothly and uniformly deposit for Na/In/C composite anode

effectively suppress Na dendrites growth and restrain the volume bulge of Na metal during long-term cycling.

### 3.4 Sodium Ion Deposition Reversibility Analysis

To obtain a better understanding of the superior sodium ion deposition reversibility on the Na/In/C electrode surface, DFT, AIMD and FE simulations were carried out to delineate the Na ion binding sites/energy, plating kinetics and deposition morphology evolution process. Initial adsorption structure models of Na–Na$_2$In and Na–NaIn

are provided in Fig. S15. As summarized in Fig. 6a-c, optimized binding energies between a Na ad-atom (blue color) and NaIn surfaces are -1.34 (100), -1.48 (110) and -1.82 eV (111), whereas these values on pure Na surfaces are -1.089 (100), -1.067 (110) and -0.761 eV (111), respectively (Fig. S16). These show that NaIn owns an intrinsic natrophilic merit and this can largely reduce Na nucleation energy and homogenize the Na$^+$ deposition flux. Meanwhile, the (311) crystal plane of Na$_2$In also shows preferable natrophilic feature as shown by its high binding energy of -1.93 eV (Fig. S17). A lattice matching (100) interface between Na and NaIn is built to further

ascertain Na ion deposition stability via AIMD simulation (Fig. 6d). As evidenced, a smooth and compact interface is sustained during the whole AIMD simulation process, thus significantly facilitating Na ion plating/stripping kinetics and removing morphological instability. In sharp contrast, porous structures are formed on the pure Na metal surface
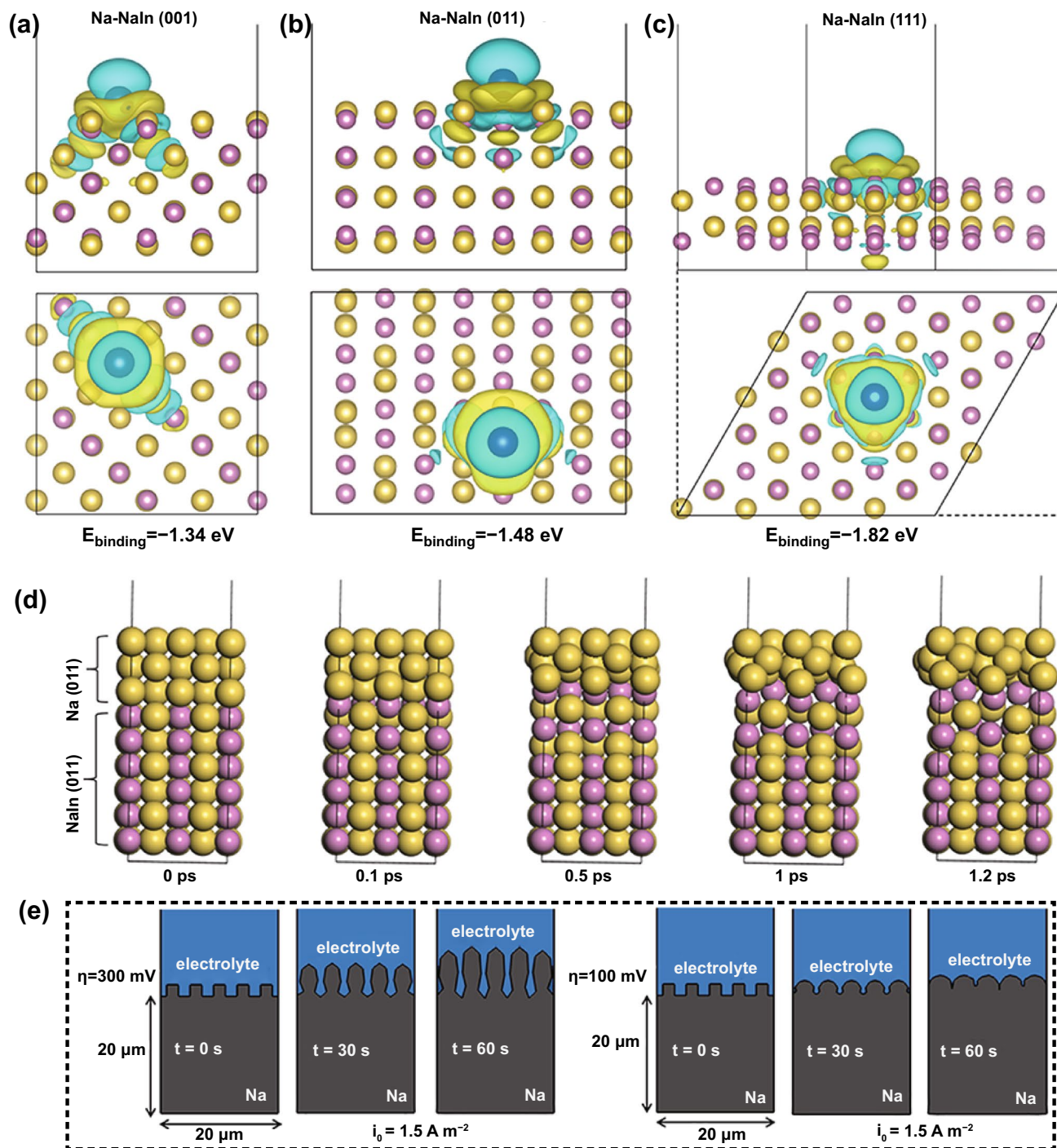


Fig. 6 **a–c** Charge differential density and the corresponding binding energies of the adsorbed Na atom on (100), (110) and (111) crystal planes of NaIn. **d** AIMD calculation results of Na ion plating kinetics on the (110) surface of NaIn at 0.1, 0.5, 1 and 2 ps. **e** Finite element simulations of Na metal electrode morphology evolution features with square-shaped bumps at an exchange density of 1.5 A m$^{-2}$ with various overpotential and time (0 s, 30 s, 60 s)

as shown in Fig. S18, which agrees well with the experimental results. Finite element simulations were further used to study evolution processes of the electrode surface at various overpotentials and time (0, 30 and 60 s). Initially, Na metal surface with square-shaped bumps was intentionally fabricated to examine Na ion deposition behavior under different overpotential (Fig. 6e). Noticeably, larger overpotential (300 meV) induces conspicuous preferential deposition, leading to severe directional growth, morphology irregularity and eventually a porous structure. However, at a lower overpotential (100 meV), unwanted porous and dendritic growth of Na metal is effectively suppressed. In addition to the effect of overpotential on Na ion deposition kinetics, initial bump shapes also play a decisive role on the Na ion plating behavior. For instance, grave dendritic growth and preferential Na ion plating occurred for the triangle-shaped bumps even at a low overpotential (100 meV), which can be ascribed to the concentrated equipotential lines at the sharp corners (Fig. S19). Adversely, the presence of regular circle-shaped bumps on the Na metal surface brought about smooth surface evolution at high 300 meV overpotential (Fig. S20). Additionally, higher exchange current density $(i_0)$ (based on the Tafel profiles analyses shown in Fig. S21a, b, $i_0$ values of the pure Na metal and the Na/In/C anode are 0.158 and 0.332 mA cm$^{-2}$, respectively) promotes smooth Na ion deposition even at larger overpotential as shown in Fig. S22 for Na/In. All these theoretical analyses evidently reveal the reversible Na ion deposition mechanism on the Na/In/C electrode (lower overpotential and larger exchange current density values) surface, matching well with prior electrochemical and chemical results.

### 3.5 Feasibility of the Na/In/C Composite Electrode in Sodium Metal Full Cell

To further elaborate the suitability of the Na/In/C composite electrode in EC/PC electrolyte (1 M NaClO$_4$ in EC/PC), Na/In/C composite and Na foil were, respectively, paired with a high-voltage Na$_3$V$_2$O$_2$(PO$_4$)$_2$F (NaVPOF) cathode to construct full coin cells. According to the area mass loading of the Na, Na/In/C and NaVPOF (experimental section) and the theoretical capacity of Na (1166 mAh g$^{-1}$)/NaVPOF (130.7

mAh g$^{-1}$, 2 ~ 4.5 V), ratios of the negative capacity to the positive capacity (N/P ratio) for the Na||NaVPOF and Na/In/C||NaVPOF full batteries are 6.2 and 4.1, respectively. XRD and SEM images of the NaVPOF cathode synthesized via a facile hydrothermal method are shown in Fig. S23a, b. Figure 7a presents specific illustration of sodium metal full batteries paired a high-voltage NaVPOF cathode with the Na/In/C composite anode. As exhibited in Fig. 7b, c, the cell demonstrates a smooth voltage profile at 0.05 C and sharp redox peaks with a scan rate of 0.5 mV s$^{-1}$ ranging from 2.5 to 4.3 V (vs Na/Na$^+$). Moreover, the NaVPOF-Na/In/C cell yields highly reversible charge capacities of 124, 115, 101, 80 and 61 mAh g$^{-1}$ at rates of 0.05, 0.1, 1, 2 and 5 C, respectively (Fig. 7d). More promisingly, the cell is observed to be able to deliver a specific capacity of 88.4 mAh g$^{-1}$ after 800 cycles with a capacity retention of 87.6% at 1 C rate, which contributes to a low capacity attenuation of 0.019% per cycle (Fig. 7e). Unsurprisingly, the NaVPOF-Na cell shows unsteady charge/discharge curve (Fig. S24a), large voltage polarization (Fig. S24b) and inferior cycling capability at 1 C (Fig. S24c). These results reinforce the much better performance of the Na/In/C composite electrode in sodium metal full batteries in the common EC/PC electrolyte.

## 4 Conclusions

In summary, a Na/In/C composite anode was synthesized by infusing metallic Na and In on a carbon cloth scaffold. As a result, symmetric cells with Na/In/C electrode manifests low-voltage hysteresis and impressive long-term cycling stability at 1 mA cm$^{-2}$ (> 870 h), 2 mA cm$^{-2}$ (> 710 h) and 5 mA cm$^{-2}$ (> 560 h), respectively, with a capacity of 1 mAh cm$^{-2}$ in a typical EC/PC electrolyte. SEM and in situ optical microscopy analyses clearly unravel that a dendrite-free and smooth morphology can be obtained in the Na/In/C composite symmetric cells. Furthermore, DFT, AIMD and FE calculations uncover the intrinsic mechanism for the reversible Na ion deposition behavior on the Na/In/C electrode. Moreover, a full sodium metal cell with a NaVPOF cathode and a Na/In/C anode presents enhanced Na ion deposition kinetics and electrochemical cycling capability. The present work offers a novel alloy strategy into the modification of Na metal chemistry for improving Na ion plating/stripping stability in the common EC/PC electrolyte.
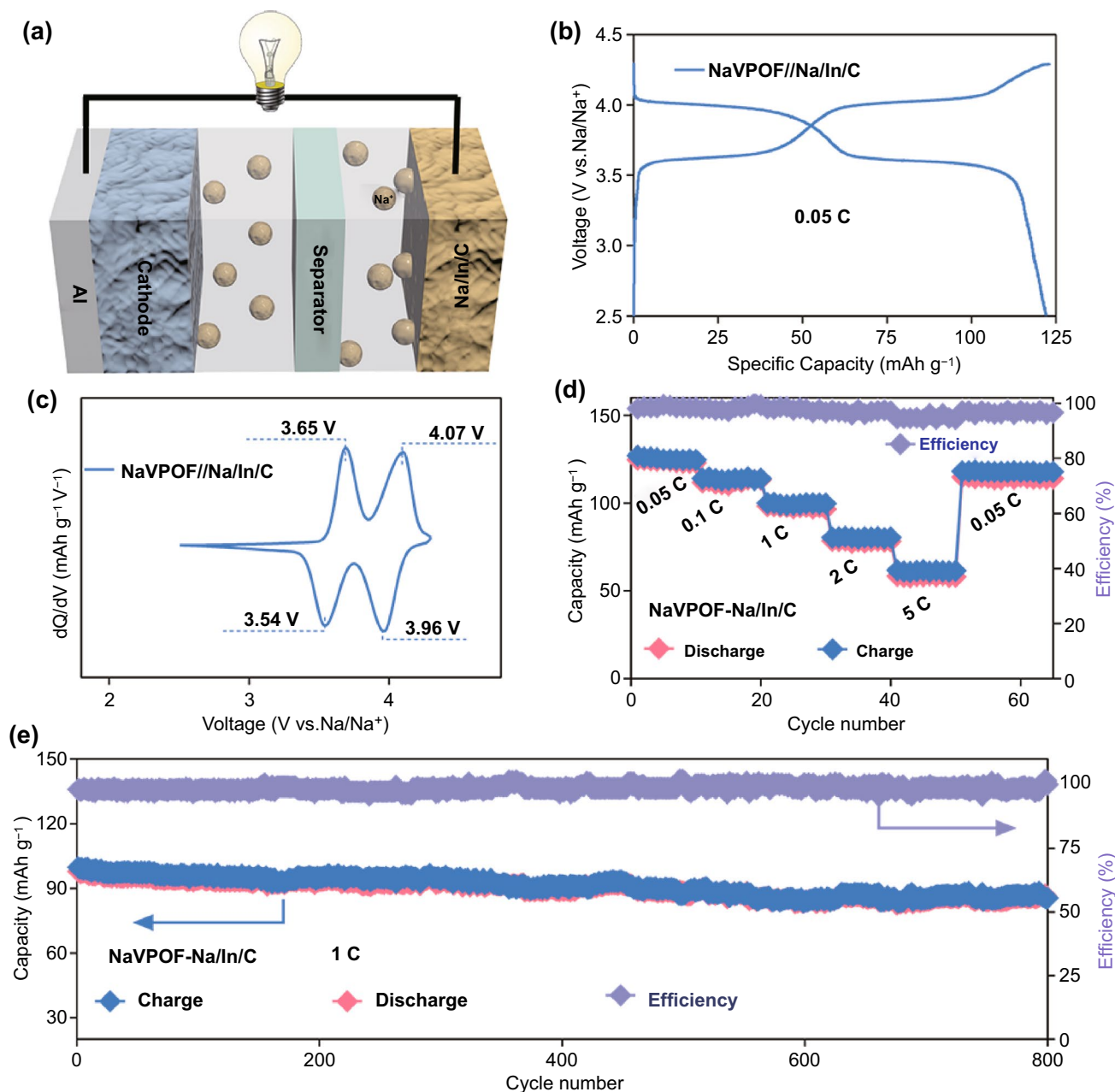
**Fig. 7** **a** Schematic illustration of a NaVPOF‖Na/In/C sodium metal full battery. Electrochemical performances of the metal full battery: **b** voltage profile; **c** CV curve at a scan rate of 0.5 mV s-1; **d** rate performance at 2.5–4.3 V; **e** long-term cycling capability at 1 C within 2.5–4.3 V

---

---

# References

1. X. Zhang, K. Chen, Z. Sun, G. Hu, R. Xiao et al., Structure-related electrochemical performance of organosulfur compounds for lithium–sulfur batteries. Energy Environ. Sci. **13**(4), 1076–1095 (2020). https://doi.org/10.1039/C9EE03848E

2. L. Hencz, H. Chen, H.Y. Ling, Y. Wang, C. Lai et al., Housing sulfur in polymer composite frameworks for Li–S batteries. Nano Micro Lett. **11**, 17 (2019). https://doi.org/10.1007/s40820-019-0249-1

3. J. Wang, Z. Zhang, X. Yan, S. Zhang, Z. Wu et al., Rational design of porous N-Ti$_3$C$_2$ MXene@CNT Microspheres for high cycling stability in Li–S battery. Nano-Micro Lett. **12**, 4 (2019). https://doi.org/10.1007/s40820-019-0341-6

4. R. Wang, R. Wu, C. Ding, Z. Chen, H. Xu et al., Porous carbon architecture assembled by cross-linked carbon leaves with implanted atomic cobalt for high-performance Li–S batteries. Nano Micro Lett. **13**, 151 (2021). https://doi.org/10.1007/s40820-021-00676-6

5. Q. Xiong, G. Huang, X.B. Zhang, High-capacity and stable Li-O$_2$ batteries enabled by a trifunctional soluble redox mediator. Angew. Chem. Int. Ed. **132**(43), 19473–19481 (2020). https://doi.org/10.1002/ange.202009064

6. Q. Lv, Z. Zhu, S. Zhao, L. Wang, Q. Zhao et al., Semiconducting metal–organic polymer nanosheets for a photoinvolved Li–O$_2$ battery under visible light. J. Am. Chem. Soc. **143**(4), 1941–1947 (2021). https://doi.org/10.1021/jacs.0c11400

7. S.H. Wang, J. Yue, W. Dong, T.T. Zuo, J.Y. Li et al., Tuning wettability of molten lithium via a chemical strategy for lithium metal anodes. Nat. Commun. **10**, 4930 (2019). https://doi.org/10.1038/s41467-019-12938-4

8. C. Jin, T. Liu, O. Sheng, M. Li, T. Liu et al., Rejuvenating dead lithium supply in lithium metal anodes by iodine redox. Nat. Energy **6**, 378–387 (2021). https://doi.org/10.1038/s41560-021-00789-7

9. T. Li, J. Sun, S. Gao, B. Xiao, J. Cheng et al., Superior sodium metal anodes enabled by sodiophilic carbonized coconut framework with 3D tubular structure. Adv. Energy Mater. **11**(7), 2003699 (2021). https://doi.org/10.1002/aenm.202003699

10. M. Zhu, G. Wang, X. Liu, B. Guo, G. Xu et al., Dendrite-free sodium metal anodes enabled by a sodium benzenedithiolate-Rich protection layer. Angew. Chem. Int. Ed. **132**(16), 6596–6600 (2020). https://doi.org/10.1002/ange.201916716

11. X. Zheng, C. Bommier, W. Luo, L. Jiang, Y. Hao et al., Sodium metal anodes for room-temperature sodium-ion batteries: applications, challenges and solutions. Energy Storage Mater. **16**, 6–23 (2019). https://doi.org/10.1016/j.ensm.2018.04.014

12. M. Guo, H. Dou, W. Zhao, X. Zhao, B. Wan et al., Three dimensional frameworks of super ionic conductor for thermodynamically and dynamically favorable sodium metal anode. Nano Energy **70**, 104479 (2020). https://doi.org/10.1016/j.nanoen.2020.104479

13. T. Yang, B. Guo, W. Du, M.K. Aslam, M. Tao et al., Design and construction of sodium polysulfides defense system for room-temperature Na–S battery. Adv. Sci. **6**(23), 1901557 (2019). https://doi.org/10.1002/advs.201901557

14. H. Wang, Y. Jiang, A. Manthiram, Long cycle life, low self-discharge sodium–selenium batteries with high selenium loading and suppressed polyselenide shuttling. Adv. Energy Mater. **8**(7), 1701953 (2018). https://doi.org/10.1002/aenm.201701953

15. T. Wu, M. Jing, L. Yang, G. Zou, H. Hou et al., Controllable chain-length for covalent sulfur–carbon materials enabling stable and high-capacity sodium storage. Adv. Energy Mater. **9**(9), 1803478 (2019). https://doi.org/10.1002/aenm.201803478

16. L. Zeng, W. Zeng, Y. Jiang, X. Wei, W. Li et al., A flexible porous carbon nanofibers-selenium cathode with superior electrochemical performance for both Li-Se and Na-Se batteries. Adv. Energy Mater. **5**(4), 1401377 (2015). https://doi.org/10.1002/aenm.201401377

17. L. Wang, X. Chen, S. Li, J. Yang, Y. Sun et al., Effect of eutectic accelerator in selenium-doped sulfurized polyacrylonitrile for high performance room temperature sodium–sulfur batteries. J. Mater. Chem. A **7**(20), 12732–12739 (2019). https://doi.org/10.1039/C9TA02831E

18. L. Fan, R. Ma, Y. Yang, S. Chen, B. Lu, Covalent sulfur for advanced room temperature sodium-sulfur batteries. Nano Energy **28**, 304–310 (2016). https://doi.org/10.1016/j.nanoen.2016.08.056

19. X. Zhao, L. Yin, T. Zhang, M. Zhang, Z. Fang et al., Heteroatoms dual-doped hierarchical porous carbon-selenium composite for durable Li–Se and Na–Se batteries. Nano Energy **49**, 137–146 (2018). https://doi.org/10.1016/j.nanoen.2018.04.045

20. Z. Li, J. Zhang, Y. Lu, X.W. Lou, A pyrolyzed polyacrylonitrile/selenium disulfide composite cathode with remarkable lithium and sodium storage performances. Sci. Adv. **4**(6), eaat1687 (2018). Doi: https://doi.org/10.1126/sciadv.aat1687

21. G. Fang, Q. Wang, J. Zhou, Y. Lei, Z. Chen et al., Metal organic framework-templated synthesis of bimetallic selenides with rich phase boundaries for sodium-ion storage and oxygen evolution reaction. ACS Nano **13**(5), 5635–5645 (2019). https://doi.org/10.1021/acsnano.9b00816

22. S.M.B. Khajehbashi, L. Xu, G. Zhang, S. Tan, Y. Zhao et al., High-performance Na–O$_2$ batteries enabled by oriented NaO$_2$

nanowires as discharge products. Nano Lett. **18**(6), 3934–3942 (2018). https://doi.org/10.1021/acs.nanolett.8b01315

23. X. Guo, W. Zhang, J. Zhang, D. Zhou, X. Tang et al., Boosting sodium storage in two-dimensional phosphorene/$Ti_3C_2T_x$ MXene nanoarchitectures with stable fluorinated interphase. ACS Nano **14**(3), 3651–3659 (2020). https://doi.org/10.1021/acsnano.0c00177

24. Y. Hu, B. Li, X. Jiao, C. Zhang, X. Dai et al., Stable cycling of phosphorus anode for sodium-ion batteries through chemical bonding with sulfurized polyacrylonitrile. Adv. Funct. Mater. **28**(23), 1801010 (2018). https://doi.org/10.1002/adfm.201801010

25. L. Li, Y. Zheng, S. Zhang, J. Yang, Z. Shao et al., Recent progress on sodium ion batteries: potential high-performance anodes. Energy Environ. Sci. **11**(9), 2310–2340 (2018). https://doi.org/10.1039/C8EE01023D

26. B. Han, Y. Zou, Z. Zhang, X. Yang, X. Shi et al., Probing the Na metal solid electrolyte interphase via cryo-transmission electron microscopy. Nat. Commun. **12**(1), 3066 (2021). https://doi.org/10.1038/s41467-021-23368-6

27. Y. Xiang, G. Zheng, Z. Liang, Y. Jin, X. Liu et al., Visualizing the growth process of sodium microstructures in sodium batteries by in-situ $^{23}$Na MRI and NMR spectroscopy. Nat. Nanotechnol. **15**(10), 883–890 (2020). https://doi.org/10.1038/s41565-020-0749-7

28. Z. Li, K. Zhu, P. Liu, L. Jiao, 3D confinement strategy for dendrite-free sodium metal batteries. Adv. Energy Mater. 2100359 (2021). Doi: https://doi.org/10.1002/aenm.202100359

29. X. Shen, R. Zhang, X. Chen, X.B. Cheng, X. Li et al., The failure of solid electrolyte interphase on Li metal anode: structural uniformity or mechanical strength? Adv. Energy Mater. **10**(10), 1903645 (2020). https://doi.org/10.1002/aenm.201903645

30. H. Wang, Z. Tong, R. Yang, Z. Huang, D. Shen et al., Electrochemically stable sodium metal-tellurium/carbon nanorods batteries. Adv. Energy Mater. **9**(48), 1903046 (2019). https://doi.org/10.1002/aenm.201903046

31. L. Zhang, X. Xia, Y. Zhong, D. Xie, S. Liu et al., Exploring self-healing liquid Na–K alloy for dendrite-free electrochemical energy storage. Adv. Mater. **30**(46), 1804011 (2018). https://doi.org/10.1002/adma.201804011

32. A. Wang, X. Hu, H. Tang, C. Zhang, S. Liu et al., Processable and moldable sodium-metal anodes. Angew. Chem. Int. Ed. **56**(39), 11921–11926 (2017). https://doi.org/10.1002/ange.201703937

33. H. Wang, C. Wang, E. Matios, W. Li, Facile stabilization of the sodium metal anode with additives: unexpected key role of sodium polysulfide and adverse effect of sodium nitrate. Angew. Chem. Int. Ed. **130**(26), 1–5 (2018). https://doi.org/10.1002/ange.201801818

34. L. Ye, M. Liao, T. Zhao, H. Sun, Y. Zhao et al., A sodiophilic interphase-mediated, dendrite-free anode with ultrahigh specific capacity for sodium-metal batteries. Angew. Chem. Int. Ed. **131**(47), 17210–17216 (2019). https://doi.org/10.1002/ange.201910202

35. J. Zheng, S. Chen, W. Zhao, J. Song, M.H. Engelhard et al., Extremely stable sodium metal batteries enabled by localized high-concentration electrolytes. ACS Energy Lett. **3**(2), 315–321 (2018). https://doi.org/10.1021/acsenergylett.7b01213

36. Y. Zhao, L.V. Goncharova, A. Lushington, Q. Sun, H. Yadegari et al., Superior stable and long life sodium metal anodes achieved by atomic layer deposition. Adv. Mater. **29**(18), 1606663 (2017). https://doi.org/10.1002/adma.201606663

37. S. Tang, Z. Qiu, X.Y. Wang, Y. Gu, X.G. Zhang et al., A room-temperature sodium metal anode enabled by a sodiophilic layer. Nano Energy **48**, 101–106 (2018). https://doi.org/10.1016/j.nanoen.2018.03.039

38. S. Choudhury, S. Wei, Y. Ozhabes, D. Gunceler, M.J. Zachman et al., Designing solid-liquid interphases for sodium batteries. Nat. Commun. **8**(1), 898 (2017). https://doi.org/10.1038/s41467-017-00742-x

39. H. Shi, M. Yue, C.J. Zhang, Y. Dong, P. Lu et al., 3D flexible, conductive, and recyclable $Ti_3C_2T_x$ MXene-melamine foam for high-areal-capacity and long-lifetime alkali-metal anode. ACS Nano **14**(7), 8678–8688 (2020). https://doi.org/10.1021/acsnano.0c03042

40. S.S. Chi, X.G. Qi, Y.S. Hu, L.Z. Fan, 3D flexible carbon felt host for highly stable sodium metal anodes. Adv. Energy Mater. **8**(15), 1702764 (2018). https://doi.org/10.1002/aenm.201702764

41. S. Lou, F. Zhang, C. Fu, M. Chen, Y. Ma et al., Interface issues and challenges in all-solid-state batteries: lithium, sodium, and beyond. Adv. Mater. **33**(6), 2000721 (2020). https://doi.org/10.1002/adma.202000721

42. Y. Lu, J.A. Alonso, Q. Yi, L. Lu, Z.L. Wang et al., A high-performance monolithic solid-state sodium battery with $Ca^{2+}$ doped $Na_3Zr_2Si_2PO_{12}$ electrolyte. Adv. Mater. **9**(28), 1901205 (2019). https://doi.org/10.1002/aenm.201901205

43. D. Lei, Y.B. He, H. Huang, Y. Yuan, G. Zhong et al., Cross-linked beta alumina nanowires with compact gel polymer electrolyte coating for ultra-stable sodium metal battery. Nat. Commun. **10**(1), 4244 (2019). https://doi.org/10.1038/s41467-019-11960-w

44. J. Zhang, D.W. Wang, W. Lv, L. Qin, S. Niu et al., Ethers illume sodium-based battery chemistry: uniqueness, surprise, and challenges. Adv. Energy Mater. **8**(26), 1801361 (2018). https://doi.org/10.1002/aenm.201801361

45. X. Liu, X. Zheng, Y. Dai, W. Wu, Y. Huang et al., Fluoride-rich solid-electrolyte-interface enabling stable sodium metal batteries in high-safe electrolytes. Adv. Funct. Mater. **31**(30), 2103522 (2021). https://doi.org/10.1002/adfm.202103522

46. P.E. Blöchl, Projector augmented-wave method. Phys. Rev. B **50**(24), 17953–17979 (1994). https://doi.org/10.1103/PhysRevB.50.17953

47. J.P. Perdew, K. Burke, M. Ernzerhof, Generalized gradient approximation made simple. Phys. Rev. Lett. **77**(18), 3865–3868 (1996). https://doi.org/10.1103/PhysRevLett.77.3865

48. S. Grimme, Semiempirical GGA-type density functional constructed with a long-range dispersion correction. J. Comput. Chem. **27**(15), 1787–1799 (2006). https://doi.org/10.1002/jcc.20495

49. J. Hutter, M. Iannuzzi, F. Schiffmann, J. VandeVondele, cp2k: atomistic simulations of condensed matter systems. WIREs Comput. Mol. Sci. **4**(1), 15–25 (2014). https://doi.org/10.1002/wcms.1159

50. G. Yoon, S. Moon, G. Ceder, K. Kang, Deposition and stripping behavior of lithium metal in electrochemical system: continuum mechanics study. Chem. Mater. **30**(19), 6769–6776 (2018). https://doi.org/10.1021/acs.chemmater.8b02623

51. B. Horstmann, J. Shi, R. Amine, M. Werres, X. He et al., Strategies towards enabling lithium metal in batteries: interphases and electrodes. Energy Environ. Sci. (2021). https://doi.org/10.1039/D1EE00767J

52. B. Lee, E. Paek, D. Mitlin, S.W. Lee, Sodium metal anodes: emerging solutions to dendrite growth. Chem. Rev. **119**(9), 5416–5460 (2019). https://doi.org/10.1021/acs.chemrev.8b00642

53. J. Liu, T. Wu, S. Zhang, D. Li, Y. Wang et al., InBr$_3$ as a self-defensed redox mediator for Li$_O$2 batteries: in situ construction of a stable indium-rich composite protective layer on the Li anode. J. Power Sources **439**, 227095 (2019). https://doi.org/10.1039/D1EE00767J